ROYAL SOCIETY OPEN SCIENCE

royalsocietypublishing.org/journal/rsos

Research

Cite this article: Koval NE, Koval P, Da Pieve F, Kohanoff J, Artacho E, Emfietzoglou D. 2022 Inelastic scattering of electrons in water from first principles: cross sections and inelastic mean free path for use in Monte Carlo track-structure simulations of biological damage. *R. Soc. Open Sci.* **9**: 212011.
https://doi.org/10.1098/rsos.212011

Received: 22 December 2021
Accepted: 19 April 2022

Subject Category:
Physics and biophysics

Subject Areas:
radiation biophysics

Keywords:
radiation damage, inelastic electron scattering, water, linear response, time-dependent density functional theory, track-structure simulations

Author for correspondence:
Natalia E. Koval
e-mail: natalia.koval.lipina@gmail.com

Downloaded from https://royalsocietypublishing.org/ on 12 July 2022

Inelastic scattering of electrons in water from first principles: cross sections and inelastic mean free path for use in Monte Carlo track-structure simulations of biological damage

Natalia E. Koval[1], Peter Koval[2], Fabiana Da Pieve[4], Jorge Kohanoff[5,6], Emilio Artacho[1,3,7,8] and Dimitris Emfietzoglou[9]

[1]CIC Nanogune BRTA, [2]Simune Atomistics SL and [3]Donostia International Physics Center DIPC, 20018 Donostia-San Sebastián, Spain
[4]Royal Belgian Institute for Space Aeronomy BIRA-IASB, 1180 Brussels, Belgium
[5]Queen's University Belfast, Belfast BT7 1NN, UK
[6]Instituto de Fusion Nuclear 'Guillermo Velarde', Universidad Politecnica de Madrid, 28006 Madrid, Spain
[7]Ikerbasque, Basque Foundation for Science, 48011 Bilbao, Spain
[8]Theory of Condensed Matter, Cavendish Laboratory, University of Cambridge, Cambridge CB3 0HE, UK
[9]Medical Physics Laboratory, University of Ioannina Medical School, 45110 Ioannina, Greece

NEK, 0000-0002-9040-0512; PK, 0000-0002-5461-2278; FDP, 0000-0001-6985-9145; JK, 0000-0002-8237-7543; EA, 0000-0001-9357-1547; DE, 0000-0002-9996-797X

Modelling the inelastic scattering of electrons in water is fundamental, given their crucial role in biological damage. In Monte Carlo track-structure (MC-TS) codes used to assess biological damage, the energy loss function (ELF), from which cross sections are extracted, is derived from different semi-empirical optical models. Only recently have first *ab initio* results for the ELF and cross sections in water become available. For benchmarking purpose, in this work, we present *ab initio* linear-response time-dependent density functional theory calculations of the ELF of liquid water. We calculated the inelastic scattering cross sections, inelastic mean free paths, and electronic stopping power and compared our results with recent calculations and experimental data showing a

© 2022 The Authors. Published by the Royal Society under the terms of the Creative Commons Attribution License http://creativecommons.org/licenses/by/4.0/, which permits unrestricted use, provided the original author and source are credited.

THE ROYAL SOCIETY PUBLISHING

Downloaded from https://royalsocietypublishing.org/ on 12 July 2022

good agreement. In addition, we provide an in-depth analysis of the contributions of different molecular orbitals, species and orbital angular momenta to the total ELF. Moreover, we present single-differential cross sections computed for each molecular orbital channel, which should prove useful for MC-TS simulations.

1. Introduction

The scattering of electrons in biological matter plays a crucial role in a variety of fields related to radiation-induced damage, such as ion-beam therapy and risk assessment in space radiation studies. In theoretical and often experimental studies of biological damage, liquid water is considered a model system. The initial response of biological material to radiation is determined, to a large extent, by the oscillator-strength distribution of its valence electrons, which leads primarily to the generation of electrons with energies of less than 100 eV [1,2]. This results from the shape of the differential cross section of molecules, which peaks at 20–30 eV and decreases to low values above 100 eV [3]. Evidence has accumulated throughout the years that very low-energy (less than 20 eV) electrons play a relevant role in bio-damage [4–8]. They constitute the so-called 'track ends' and are reported to have an increased biological effectiveness [9–11]. Experiments have indicated that electrons (or photons) with energies as low as few electron-volts can still induce double-strand breaks, possibly through a resonance mechanism [12–14].

Nowadays, several Monte Carlo track-structure (MC-TS) codes exist [15–18], able to describe the transport of electrons via an event-by-event simulation until low energy (approx. 10 eV), like NOREC [19], KURBUC [20], PARTRAC [21], RITRACKS [22] and the open source Geant4-DNA [23,24]. The track structures in water are then overlaid onto DNA models ranging in complexity from simple cylindrical models of the DNA to a full atomistic description of human chromosomal DNA [25–29]. MC-TS codes either rely on pre-parameterized sets of cross sections [1] or use optical data models for the dielectric function of water based on the first Born approximation [30–34]. In such models, the energy loss function (ELF) in the dielectric formalism, from which other quantities like cross sections and inelastic mean free path (IMFP) are calculated, is determined at negligible momentum transfer $q = 0$ from experimental data (often optical data [35,36]). For finite momentum transfers $q \neq 0$, the ELF is appropriately extended to the whole Bethe surface via dispersion models based on the electron gas theory [15] within the context of the random-phase approximation (RPA). The ELF is commonly described via a superposition of either normal or derivative Drude functions. The Drude model parameters associated with the height, width and position of the peaks are used as adjustable parameters determined by the fit to experimental data and are generally constrained by sum rules. Other models exist as well, based on Mermin functions [37], which partially incorporate effects beyond RPA.

By assuming that each electron interacts with the average field generated by all other electrons, the RPA accounts only for electrostatic screening. The exchange-correlation (XC) effects (due to the instantaneous Coulomb repulsion and the Pauli exclusion principle) are neglected in RPA. The Born approximation neglects, among other things, exchange effects between the incident and struck electrons. For high energies, such effects are only important for hard collisions, characterized by a large energy transfer. At low energies, however, the incident and the target electrons have similar energies and thus one expects that exchange effects will become relevant essentially for all collisions. Moreover, in the Born approximation, a first-order perturbation theory is used to describe the interaction between the projectile and the target, which is in principle not valid for low energies [38,39]. The use of approximations for the scattering parameters leads to differences in simulations of track structure [40]. The discrepancies in the inelastic scattering obtained with different extension algorithms to extrapolate optical data to finite momentum transfer can reach a factor of about two in the range 50–200 eV (and even larger at still lower energies) [41]. Recent studies have reported a potentially relevant effect of the different dielectric function implementations on ionization clustering [42] and DNA damage induction [43].

There is a high degree of uncertainty in the low-energy range in MC-TS codes as the cross sections become sensitive to the details of the electronic structure of the target [44–47]. Even though atomic structures are implemented in some TS codes [48–50], the absence of electronic effects and often occurring lack of reference cross sections for benchmarking make it difficult to extend the applicability of such codes to the targets other than homogeneous liquid water. In fact, codes like Geant4-DNA use the cross sections for water independently of the actual medium, only re-scaling the density.

Downloaded from https://royalsocietypublishing.org/ on 12 July 2022

Several recent works have been performed to ameliorate the description of the dielectric function and the IMFP of water. One way is to include the XC effects beyond RPA on the basis of the electron gas model [39,51]. Other works additionally tried improving the effects beyond the first Born approximation [29,52], improving previous dispersion algorithms [53], developing new TS codes [54,55] and clarifying differences in inelastic scattering between different condensed phases [56]. Others focus on extending the set of cross sections for electron scattering in targets other than water via pre-parameterized models [57] or multi-channel and R-matrix approaches [58].

Overall, the accuracy of the semi-empirical results for water at energies below 100 eV remains questionable. *Ab initio* calculations can provide insightful results for the dielectric function, the electron ELF and the IMFP in the whole energy range. First-principles methods do not rely on any free parameters and thus have predictive power and can be extended to a variety of targets. Nowadays, time-dependent density functional theory (TDDFT) [59,60] is the method of choice for the study of excited states, since it allows for the affordable extraction of physical information without *a priori* assumptions on the system and on the knowledge of associated cross sections. TDDFT can be formulated either in the perturbative regime [61] or via an explicit solution of the time-dependent Kohn–Sham (KS) equations [62,63] by propagating the KS orbitals in real time. Nevertheless, *ab initio* studies on the ELF and IMFP in water for low-energy electrons are limited so far. A previous real-time TDDFT study by Tavernelli [64] presented a dielectric constant of liquid water (optical limit only) with two prominent peaks as opposed to only one main peak in the experimental data [41]. A more recent work by Taioli *et al.* [65] presented linear-response TDDFT (LR-TDDFT) calculations of the ELF for liquid water. The sample of 32 molecules was obtained from a larger sample generated via classical molecular dynamics simulations and then optimized via DFT. The XC effects were considered in the adiabatic generalized gradient approximation (AGGA). The ELF obtained in Taioli *et al.* [65] has shown a good agreement with experiments. However, the orbital analysis of the ELF has not been performed in the *ab initio* framework.

In this work, we performed a detailed first-principles investigation of the electron scattering in liquid water both in the optical limit and for finite momentum transfer. Using an efficient iterative method based on LR-TDDFT and a linear combination of atomic orbitals (LCAO) incorporated in the MBPT-LCAO code [66,67], we calculated the ELF of liquid water in a range of finite values of the momentum transfer. The electron–electron interactions were considered at the RPA level in the linear response, unlike in the work by Taioli *et al.* [65], who used the AGGA. RPA yields the correct asymptotic behaviour for the long-range interactions absent in AGGA [68]. The inelastic scattering cross sections, the IMFP and the electronic stopping power of electrons in water were then calculated from the ELF using analytical expressions [34,51]. Furthermore, we performed a detailed analysis of the contributions of molecular orbitals, chemical species and their pairs, as well as orbital angular momenta to the ELF. Additionally, we computed the cross sections for different molecular orbital channels which can benchmark semi-empirical calculations. Apart from the results presented in this article, we provide the data at https://doi.org/10.5061/dryad.d51c5b057 for the peruse in MC-TS simulations.

2. Methodology

2.1. Linear-response time-dependent density functional theory calculations with MBPT-LCAO

The ELF is the fundamental quantity that defines the scattering properties of a material. It is defined as the imaginary part of the inverse macroscopic dielectric function ϵ_{M} [69]:

$$\mathrm{ELF}(E, \mathbf{q}) = \mathrm{Im}\left[\frac{-1}{\epsilon_{\mathrm{M}}(E, \mathbf{q})}\right], \tag{2.1}$$

which relates the external perturbation (potential) V^{ext} and the total potential V^{tot} acting in a system: $V^{\mathrm{ext}}(E, \mathbf{q}) = \epsilon_{\mathrm{M}}(E, \mathbf{q})V^{\mathrm{tot}}(E, \mathbf{q})$.

In LR-TDDFT (see [70] for a broad overview), the main quantity that gives all the information about the response of a solid to an external perturbation V^{ext} is the microscopic dielectric function ϵ. The macroscopic dielectric function can be obtained from the microscopic one using the so-called macroscopic averaging, i.e. by averaging the microscopic quantities over all the unit cells, since macroscopic quantities slowly vary over the unit cell while microscopic ones vary rapidly [71]:

$$\epsilon_{\mathrm{M}}(E, \mathbf{q}) = \frac{1}{\epsilon^{-1}_{\mathbf{G}=0,\mathbf{G}'=0}(E, \mathbf{q})} \neq \epsilon_{\mathbf{G}=0,\mathbf{G}'=0}(E, \mathbf{q}). \tag{2.2}$$

Downloaded from https://royalsocietypublishing.org/ on 12 July 2022

Here, **G, G′** are lattice vectors in the reciprocal space, which is more convenient to use when dealing with periodic systems. The differences between microscopic and averaged (macroscopic) fields are called the crystal local fields, or local field effects (LFE).

The inverse microscopic dielectric function is related to the interacting linear-response function $\chi_{\mathbf{GG'}}(E, \mathbf{q}) = \delta n_{\mathbf{G}}(E, \mathbf{q})/\delta V^{\text{ext}}_{\mathbf{G'}}(E, \mathbf{q})$, an operator producing the induced density δn in response to a change of an external potential δV^{ext}:

$$\epsilon^{-1}_{\mathbf{GG'}}(E, \mathbf{q}) = \delta_{\mathbf{GG'}} + \upsilon_{\mathbf{GG''}}(\mathbf{q})\chi_{\mathbf{G''G'}}(E, \mathbf{q}), \tag{2.3}$$

where $\upsilon_{\mathbf{GG'}}(\mathbf{q}) = 4\pi\delta_{\mathbf{GG'}}/|\mathbf{q}+\mathbf{G}|^2$ is the Coulomb interaction matrix element between plane waves and $\delta_{\mathbf{GG'}}$ is the Kronecker delta symbol. We adopt the repeated index sum convention in this section. Thus, the ELF in terms of the interacting response function reads

$$\text{ELF}(E, \mathbf{q}) = -\frac{4\pi}{q^2}\text{Im}\chi_{\mathbf{G}=0,\mathbf{G'}=0}(E, \mathbf{q}). \tag{2.4}$$

In the KS formalism, the external potential is related to an effective potential $V^{\text{eff}}(\mathbf{r}, t) \equiv V^{\text{ext}}(\mathbf{r}, t) + V^{\text{Hxc}}(\mathbf{r}, t)$, where Hxc stands for Hartree + XC potential—the relation generating a Dyson-type equation for the interacting $\chi_{\mathbf{GG'}}(E, \mathbf{q})$ and non-interacting $\chi^0_{\mathbf{GG'}}(E, \mathbf{q})$ response functions [72]:

$$\chi_{\mathbf{GG'}}(E, \mathbf{q}) = \chi^0_{\mathbf{GG'}}(E, \mathbf{q}) + \chi^0_{\mathbf{GG''}}(E, \mathbf{q})K^{\mathbf{G''G'''}}(\mathbf{q})\chi_{\mathbf{G'''G'}}(E, \mathbf{q}). \tag{2.5}$$

The crucial ingredient here is the interaction kernel $K^{\mathbf{GG'}}(\mathbf{q})$, given by

$$K^{\mathbf{GG'}}(\mathbf{q}) = \upsilon_{\mathbf{GG'}}(\mathbf{q}) + f_{\text{xc};\mathbf{GG'}}(\mathbf{q}). \tag{2.6}$$

The XC kernel f_{xc} is the functional derivative of the time-dependent XC potential with respect to the time-dependent particle density and $\upsilon_{\mathbf{GG'}}$ is the functional derivative of the Hartree potential with respect to the density. In this work, we calculated the LR-TDDFT interaction kernel $K^{\mathbf{GG'}}(\mathbf{q})$ in the RPA approximation $K^{\mathbf{GG'}}(\mathbf{q}) = \upsilon_{\mathbf{GG'}}$. The XC effects are only taken into account in the ground state calculations. The RPA response function, only accounting for the Hartree component of the induced potentials, generally provides a good description of long-range screening [73].

The non-interacting response function appearing in equation (2.5) can be calculated as follows [71,74]:

$$\chi^0_{\mathbf{GG'}}(E, \mathbf{q}) = \frac{1}{N_{\text{k}}}\sum_{\text{n,m,}\mathbf{k}}\frac{(f_{\text{n},\mathbf{k}} - f_{\text{m},\mathbf{k}+\mathbf{q}})U^{\mathbf{G}}_{\text{nm},\mathbf{k}}(\mathbf{q})\overline{U}^{\mathbf{G'}}_{\text{nm},\mathbf{k}}(\mathbf{q})}{E - (\mathcal{E}_{\text{m},\mathbf{k}+\mathbf{q}} - \mathcal{E}_{\text{n},\mathbf{k}}) + \text{i}\eta}. \tag{2.7}$$

Here, $f_{\text{n},\mathbf{k}}$ and $\mathcal{E}_{\text{n},\mathbf{k}}$ are the occupation numbers and the energies of the corresponding KS eigenstates, η is a broadening constant and N_{k} is the number of k-points in the chosen Brillouin zone (BZ) sampling. $U^{\mathbf{G}}_{\text{nm}}(\mathbf{k}, \mathbf{q})$ are the matrix elements of plane waves in the basis of KS eigenstates $\Psi_{\text{n},\mathbf{k}}(\mathbf{r})$

$$U^{\mathbf{G}}_{\text{nm},\mathbf{k}}(\mathbf{q}) = \frac{1}{\sqrt{V_{\text{uc}}}}\int \Psi^*_{\text{n},\mathbf{k}}(\mathbf{r})\text{e}^{-\text{i}(\text{G}+\mathbf{q})\mathbf{r}}\Psi_{\text{m},\mathbf{k}+\mathbf{q}}(\mathbf{r})\,\text{d}^3r, \tag{2.8}$$

where V_{uc} is the unit cell volume.

The MBPT-LCAO code uses an efficient iterative Krylov-subspace method to calculate the ELF (equation (2.4)). More details about the LR-TDDFT implementation in the MBPT-LCAO code can be found in [66].

2.2. Partition of the electron energy loss function

The non-interacting response function $\chi^0_{\mathbf{GG'}}(E, \mathbf{q})$ has an explicit expression in terms of KS orbitals $\Psi_{\text{n},\mathbf{k}}(\mathbf{r})$, their eigenenergies $\mathcal{E}_{\text{n},\mathbf{k}}$ and occupations $f_{\text{n},\mathbf{k}}$ (equations (2.7) and (2.8)). To analyse the contribution of different orbitals, as well as different species to the total ELF, we will express the ELF via the non-interacting response function. For this, it is convenient to rewrite equation (2.5) in the following form:

$$\chi = \chi^0[\delta - K\chi^0]^{-1}. \tag{2.9}$$

The operator $[\delta - K\chi^0]^{-1}$converts the external potential $V^{\text{ext}}_{\mathbf{G}+\mathbf{q}}(E)$ to an effective potential $V^{\text{eff}}_{\mathbf{G}+\mathbf{q}}(E)$. In our case, $V^{\text{ext}}_{\mathbf{G}+\mathbf{q}}(E) \equiv \delta_{\text{G},0}$ and the effective potential $V^{\text{eff}}_{\mathbf{G}+\mathbf{q}}(E)$ is computed by solving

$$[\delta_{\mathbf{GG'}} - K_{\mathbf{GG''}}\chi^0_{\mathbf{G''G'}}(E, \mathbf{q})]V^{\text{eff}}_{\mathbf{G'}+\mathbf{q}}(E) = V^{\text{ext}}_{\mathbf{G}+\mathbf{q}}(E). \tag{2.10}$$

Downloaded from https://royalsocietypublishing.org/ on 12 July 2022

In what is described in §2.1, the computation of the ELF is performed by applying the non-interacting response to the effective potential:

$$\mathrm{ELF}(E, \mathbf{q}) = -\frac{4\pi}{q^2}\mathrm{Im}\chi^0_{\mathbf{G}=\mathbf{0},\mathbf{G}'}(E, \mathbf{q})V^{\mathrm{eff}}_{\mathbf{G}'+\mathbf{q}}(E). \tag{2.11}$$

Summing over the reciprocal lattice vectors $\mathbf{G}'$, we get

$$\mathrm{ELF}(E, \mathbf{q}) = -\frac{4\pi}{q^2}\mathrm{Im}\sum_{\mathrm{n,m,k}} U_{\mathrm{nm,k}}(\mathbf{q})D_{\mathrm{nm,k}}(E, \mathbf{q}), \tag{2.12}$$

where

$$U_{\mathrm{nm,k}}(\mathbf{q}) = \int \Psi^*_{\mathrm{n,k}}(\mathbf{r})\mathrm{e}^{-\mathrm{i}\mathbf{q}\mathbf{r}}\Psi_{\mathrm{m,k+q}}(\mathbf{r})\,\mathrm{d}^3r \tag{2.13}$$

and

$$D_{\mathrm{nm,k}}(E, \mathbf{q}) = \sum_{\mathbf{G}'}(f_{\mathrm{n,k}} - f_{\mathrm{m,k+q}}) \times \frac{\int \Psi^*_{\mathrm{m,k+q}}(\mathbf{r})\mathrm{e}^{\mathrm{i}(\mathbf{G}'+\mathbf{q})\mathbf{r}}\Psi_{\mathrm{n,k}}(\mathbf{r})\,\mathrm{d}^3r}{E - (\mathcal{E}_{\mathrm{m,k+q}} - \mathcal{E}_{\mathrm{n,k}}) + \mathrm{i}\eta} V^{\mathrm{eff}}_{\mathbf{G}'+\mathbf{q}}(E). \tag{2.14}$$

Since equation (2.12) is linear in all the indices, we can split the ELF into different contributions. For example, the contributions of the electron–hole pairs can be defined as

$$\mathrm{ELF}_{\mathrm{nm,k}}(E, \mathbf{q}) = -\frac{4\pi}{q^2}\mathrm{Im}\,[U_{\mathrm{nm,k}}(\mathbf{q})D_{\mathrm{nm,k}}(E, \mathbf{q})]. \tag{2.15}$$

In practice, when the (atomistic) system is large and consists of many almost equal parts (water model), it is desirable to estimate the contributions of different (crystalline) orbitals defined by their energies $\mathcal{E}_{\mathrm{n,k}}$ to the total ELF(E, $\mathbf{q}$). This is achieved by defining an occupied-energy differential ELF (DELF):

$$\mathrm{DELF}^{\mathrm{occ}}(E, \mathbf{q}, \mathcal{E}) = \sum_{\mathrm{n<m}} \delta(\mathcal{E} - \mathcal{E}_{\mathrm{n,k}})\mathrm{ELF}_{\mathrm{nm,k}}(E, \mathbf{q}) + \sum_{\mathrm{m<n}} \delta(\mathcal{E} - \mathcal{E}_{\mathrm{m,k+q}})\mathrm{ELF}_{\mathrm{nm,k}}(E, \mathbf{q}). \tag{2.16}$$

The contributions of different angular momenta, species or combination of these can be 'tracked' using an expansion of the KS orbitals in terms of the atomic orbitals:

$$\Psi_{\mathrm{n,k}}(\mathbf{r}) = \sum_a C^a_{\mathrm{n,k}}\phi^a(\mathbf{r}, \mathbf{k}), \tag{2.17}$$

where $C^a_{\mathrm{n,k}}$ are the LCAO coefficients and $\phi^a(\mathbf{r}, \mathbf{k})$ are the Bloch-symmetric atomic orbitals. The atomic orbital index a is connected to particular atoms, angular momenta, etc.

2.3. Inelastic scattering cross sections and stopping power from the energy loss function

As has been mentioned above, all the relevant quantities in the inelastic electron scattering can be calculated from the ELF [34,51]. According to the non-relativistic plane-wave Born approximation, the double-differential inelastic scattering cross section is defined as follows:

$$\frac{\mathrm{d}^2\Sigma(E, q; T)}{\mathrm{d}E\mathrm{d}q} = \frac{1}{\pi a_0 T q}\mathrm{ELF}(E, q), \tag{2.18}$$

where T is the incident electron kinetic energy, a_0 is the Bohr radius. Note that here we used the magnitude q of the momentum transfer vector $\mathbf{q}$ since it is expected to be isotropic in liquid water (and our tests confirm this for our sample; see figure 13 in appendix A).

The single-differential cross section (SDCS) can be obtained from (2.18) by integrating over momentum transfer q:

$$\frac{\mathrm{d}\Sigma(E; T)}{\mathrm{d}E} = \frac{1}{\pi a_0 T}\int_{q_{\mathrm{min}}(E;T)}^{q_{\mathrm{max}}(E;T)} \frac{\mathrm{ELF}(E, q)}{q}\,\mathrm{d}q, \tag{2.19}$$

where the limits $q_{\mathrm{min/max}}(E; T) = \sqrt{2m}\left(\sqrt{T} \mp \sqrt{T - E}\right)$ come from momentum conservation (m is the electron rest mass).

Downloaded from https://royalsocietypublishing.org/ on 12 July 2022

The total inelastic cross section Σ (also called inverse IMFP) and the electronic (or collisional) stopping power S_e are defined as

$$\Sigma(T) = \int_{E_{min}}^{E_{max}(T)} \frac{d\Sigma(E;T)}{dE}\, dE \tag{2.20}$$

and

$$S_e(T) = -\frac{dT}{dx} = \int_{E_{min}}^{E_{max}(T)} E\frac{d\Sigma(E;T)}{dE}\, dE, \tag{2.21}$$

with the maximum energy loss by an electron with energy T being $E_{max} = \min[(T + E_{gap})/2,\ T - E_F]$ for insulators, where E_{gap} is the energy gap of the target, and E_F is the Fermi energy; and the minimum defined as $E_{min} = E_{gap}$ [47,51]. Note that this assumes that electronic excitation can only occur for energies larger than the gap, which acts as an effective threshold. However, recent studies have shown that this is possible also for energies below the gap [75,76]. Here, we go beyond the threshold, i.e. use the limit $E_{min} = 0$ in equations (2.20) and (2.21).

3. Numerical details

3.1. SIESTA single-point and MBPT-LCAO calculations

The ground state KS orbitals of the water samples needed as a starting point for the LR-TDDFT calculations were obtained using the static DFT as implemented in the SIESTA code [77] using periodic boundary conditions. A $2 \times 2 \times 2$ Monkhorst–Pack [78] k-point mesh was used in the SIESTA calculations. The XC functional in the local-density approximation (LDA) in the Ceperley–Alder form [79] was used. Norm-conserving Troullier–Martins [80] pseudopotentials were used to replace the core electrons. Basis sets of different sizes, i.e. single-, double- and triple-ζ polarized (SZP, DZP and TZP, respectively), with an energy shift of 20 meV were used in the test runs, and then the TZP basis set was chosen to perform the calculations of cross sections, IMFP and stopping power.

In the LR-TDDFT calculations, q cannot take values smaller than the distance between two k-points in the BZ. This distance can be estimated as $2\pi/(n_k a)$, where a is the lattice constant and n_k is the number of k-points in a particular direction. For a BZ sampling of $[3 \times 3 \times 3]$ k-points used in our calculations, we approximated the optical limit by $q_0 = 0.1$ a.u. We have calculated ELF for a total of 20 values of q in the interval [0.1 : 2.0] a.u. The resolution in energy loss was defined by $\Delta E = 0.15$ eV and the broadening constant $\eta = 0.3$ eV (a sensible value must be $\geq 2\Delta E$).

3.2. Water samples

The results presented in §§4.1 and 4.2 were calculated for a water sample denoted as PBE-64 (referring to the XC functional and the number of water molecules) shown in figure 1*a*. The sample PBE-64 is composed of 64 water molecules which were initially randomly placed inside a cubic cell with a lattice constant $a = 12.45$ Å, giving a density of 0.995 g cm^{-3}. The structure was equilibrated using Born–Oppenheimer molecular dynamics (BOMD) using the SIESTA code [77]. The BOMD simulations were performed for a total time of 2.5 ps at a temperature of 300 K in the NVT ensemble (Nosé thermostat) with default Nosé mass of 100 Ry fs^2. A time step of 0.5 fs was used in the calculations. A DZP basis set of numerical atomic orbitals was used in the SIESTA BOMD simulations [81,82]. The cut-off radii of the first-ζ functions were defined by an energy shift of 20 meV. The second-ζ radii were defined by a split norm of 0.3. Soft confining potentials of 40 Ry with default inner radius of 0.9 were used in the basis-set generation [82]. The plane-wave cut-off for the real-space grid was defined by a mesh cut-off of 300 Ry. The self-consistency was controlled by a convergence parameter of 10^{-3} eV for the Hamiltonian matrix elements. The generalized gradient approximation (GGA) in the PBE [83] form was used to account for the XC effects.

The calculations presented in §§4.3 and 4.4 were performed for the water sample PBE-16 (figure 1*b*) composed of 16 water molecules to reduce the computational cost. The sample PBE-16 was optimized using BOMD with the same parameters as the sample PBE-64.

A few additional water samples of different sizes, atomic configurations and equilibrated with different XC functionals were used for testing purposes (see details in appendix A).

Downloaded from https://royalsocietypublishing.org/ on 12 July 2022

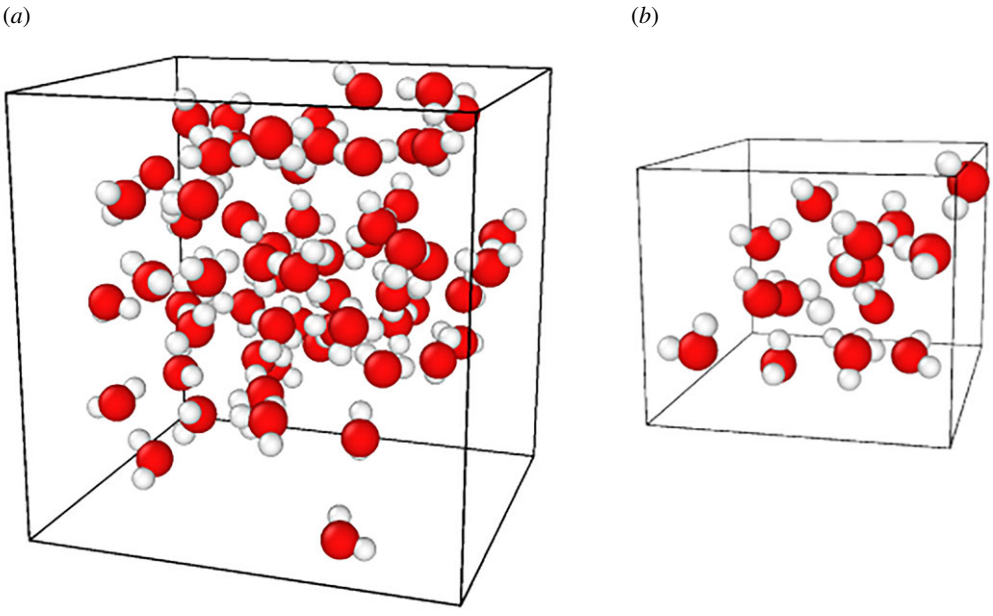

Figure 1. Unit cells of (*a*) PBE-64 and (*b*) PBE-16 water samples.

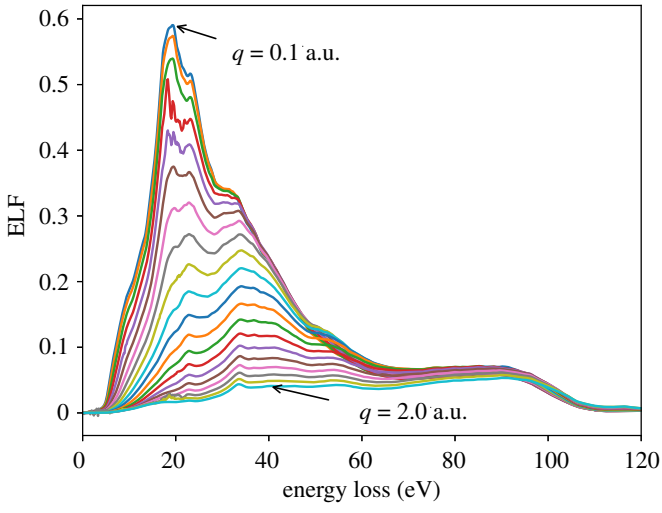

Figure 2. ELF of liquid water (a.u.) as a function of energy loss (eV) calculated with LR-TDDFT for $q = [0.1 : 2.0]$ a.u. The PBE-64 water sample and TZP basis set were used in all calculations.

4. Results and discussion

4.1. Energy loss function

The ELF for different values of the momentum transfer is shown in figure 2 as a function of energy loss. The ELF exhibits a clear evolution for different values of the momentum transfer. At small q, a defined feature (i.e. a single maximum, accompanied by some shoulders) is clearly visible associated with the optical excitations sensitive to the optical band gap. For larger q, the energy loss involves larger wavevector excitations linked to the band structure of the system.

Figure 3 shows the comparison of our results for the momentum transfer of 0.1 and 1 a.u. with inelastic X-ray scattering (IXS) experimental data [36]. A convergence test for the ELF with respect to the basis set size is presented as well. The DZP and TZP results for the ELF at $q = 0.1$ a.u. are almost identical. At $q = 1.0$ a.u., the DZP and TZP slightly vary, with TZP closer reproducing main experimental features around the maximum of the ELF. Main panels show the results obtained

Downloaded from https://royalsocietypublishing.org/ on 12 July 2022

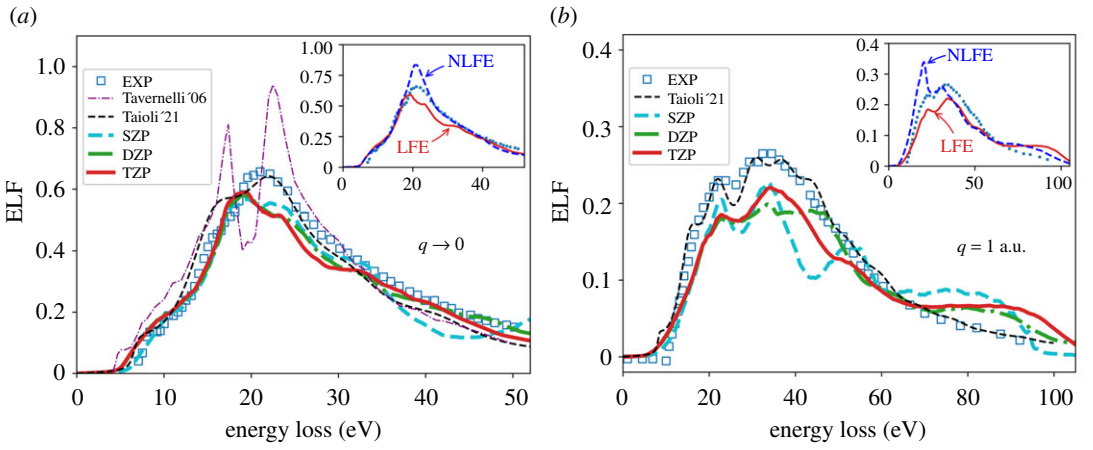

Figure 3. ELF of liquid water: (*a*) in the optical limit $q = 0.1$ a.u. and (*b*) for the momentum transfer $q = 1.0$ a.u. as a function of energy loss (eV) calculated with LR-TDDFT for PBE-64 water sample using different basis set sizes (SZP, DZP and TZP) in the SIESTA calculations as indicated for each line. LR-TDDFT results are compared to the experimental data obtained via IXS spectroscopy data [36] and to calculations by Tavernelli [64] (for $q \to 0$) and Taioli *et al.* [65]. Insets show the ELF with and without local field effects (LFE and NLFE, respectively) compared to experiment.

including the LFE, while the insets compare the results obtained with and without the LFE to the experimental data.

In the optical limit (figure 3*a*), the tails of the ELF from IXS experiments are well reproduced by our well-converged (TZP) calculations. The main peak is slightly underestimated and appears slightly shifted to lower energy loss values as compared to the experiment. The results of Tavernelli [64] obtained with real-time TDDFT (RT-TDDFT) are also shown in figure 3*a* and, as has been mentioned before, the RT-TDDFT ELF shows two maxima with a minimum located at similar energy loss values as the experimental maximum.

Recent calculations by Taioli *et al.* [65] obtained with LR-TDDFT (including XC effects in the AGGA) are also shown in figure 3. The main peak is captured well by Taioli *et al.* [65]; however, a feature at $E \approx 15$ eV is higher than in the experimental ELF, and the main peak shows two features (although much less prominent) similar to the results of Tavernelli. Thus, our RPA results better reproduce both the lower and higher energy-loss side of the main peak, while the AGGA results from Taioli *et al.* [65] better reproduce the main peak. Often, RPA with LFE is able to reproduce fairly well the energy loss spectra at $q = 0$ [84]. AGGA generally brings an improvement upon RPA in finite systems [85]. However, for extended non-metallic systems, the XC-kernel effect vanishes due to the absence of the long-range ($1/r$) decay [85–87] and thus AGGA yields a relatively small correction to the RPA results [88,89]. The inclusion of the LFE, however, plays a significant role in the correct description of the electron energy loss [88], as proven by our results.

At finite value of the momentum $q = 1$ a.u., positions of experimental peaks and their widths are well captured by our calculations (figure 3*b*). However, the height is slightly underestimated and there is a plateau at high energy loss in the calculated ELF which is not present in the experimental data. Taioli *et al.* [65] do not get such plateau in their calculations and they capture the height and width of the peaks quite accurately. Overall, this comparison clearly confirms, in a TDDFT framework and considering the system beyond an electron gas as done in optical data models for TS calculations, that considering XC effects is more important for finite momentum transfer, as already anticipated by previous works in optical data models [41].

Apart from intensities and position of the peaks, one should also discuss the 'fall off' on the sides of the main structure. The extension algorithms used in many MC TS codes (e.g. in Geant4-DNA [23]) do not account for the momentum broadening of the ELF being largely based on the early Ritchie model(s) and the Ashley model, which exhibit a much steeper fall below the maximum. However, more recent MC TS codes have included momentum broadening either empirically [51] or via the Mermin dielectric function [90].

In the insets to figure 3, we compare the ELF obtained with the LFE, which is the same as the TZP results of the main panels, and without LFE (i.e. NLFE). In an inhomogeneous and polarizable system, on a microscopic scale, the LFE imply that the matrix $\epsilon_{GG'}$ has non-zero off-diagonal elements. In practical terms, it means that the Coulomb interactions between the electrons of the

Downloaded from https://royalsocietypublishing.org/ on 12 July 2022

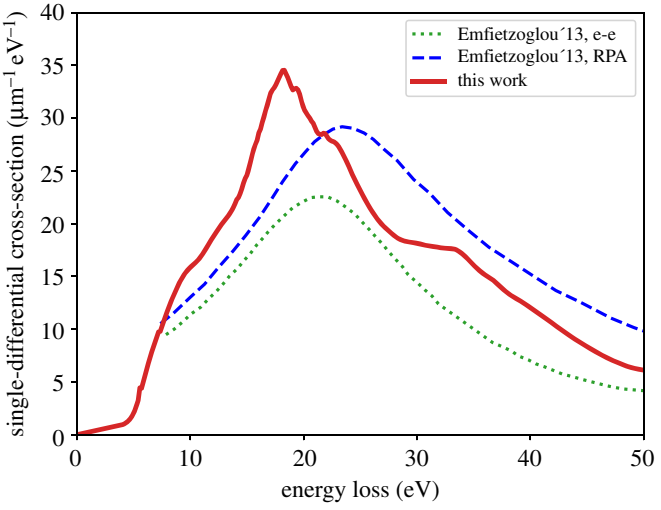

Figure 4. Single-differential cross section (equation (2.19)) for incident electron kinetic energy $T = 100$ eV. Results from Emfietzoglou *et al.* [51] are shown for comparison.

system (i.e. the Coulomb kernel, equation (2.6)) are included. The LFE are stronger when the inhomogeneity of the system is larger. Although, if the microscopic polarizability of the inhomogeneous system is small, the LFE are small. For $q \to 0$, the LFE only change the height of the main feature (inset to figure 3*a*), maintaining to a large extent the overall shape of the NLFE result. Practically, the LFE suppress the absorption, due to the induced classical depolarization potential. LFE are expected to give a small contribution in situations and systems with a smoothly varying electronic density. On the contrary, the LFE give a more sizable contribution for larger wavevectors as seen in the inset to figure 3*b*.

4.2. Inelastic scattering cross sections and electronic stopping power

Understanding the energy (and angle) distribution of secondary electrons is fundamental for characterizing the physical step of radiation bio-damage. Indeed, such energy will determine not only the specific processes by which such electrons will interact with the biological molecules in the water solvent, but also how close bond-breaking events, possibly occurring at nucleobase pairs or at the sugar–phosphate chain, occur (clustering). Depending on the clustering of these events, the damage may be irreparable. Here, we present the calculated single-differential as well as total inelastic scattering cross sections and compare our results with the calculations from the dielectric formalism. The IMFP and the stopping power are also compared to the results from the default, Ioannina and CP100 models as implemented in Geant4-DNA.

Figure 4 shows the SDCS calculated using equation (2.19) for the electron kinetic energy $T = 100$ eV in comparison with different approximations of the Emfietzoglou model [51]. The label 'e-e' in Emfietzoglou *et al.* [51] results stands for the semi-empirical electron–electron dielectric function representing an XC corrected screened interaction between the incident and struck electrons. The label 'RPA' stands for the random-phase approximation within the Lindhard formalism for dielectric function obtained under the plasmon-pole approximation for a homogeneous electron gas. Further details can be found in Emfietzoglou *et al.* [51]. The maximum of SDCS obtained in this work is shifted to lower values of the energy loss when compared with the semi-empirical results. Overall, the agreement is qualitative. The SDCS for electron kinetic energies of 500 eV, 1 keV and 5 keV are given in appendix A (figure 14).

The total inelastic cross section is shown in figure 5 and compared to the results of Emfietzoglou *et al.* [51], de Vera *et al.* [92] and Taioli *et al.* [65], as well as with experimental data for amorphous ice. Here, the total cross section is expressed in the units of inverse length, i.e. the conventional units of length squared multiplied by the number density of the target atoms [51]. Our result agrees with the RPA model of Emfietzoglou *et al.* being slightly higher at intermediate electron energies. Both RPA calculations, our LR-TDDFT and the Emfietzoglou model, converge to the experimental curve only at energies below 20 eV. Recent LR-TDDFT results from Taioli *et al.* [65] are slightly higher than ours, but become similar at energies above 80 eV.

Downloaded from https://royalsocietypublishing.org/ on 12 July 2022

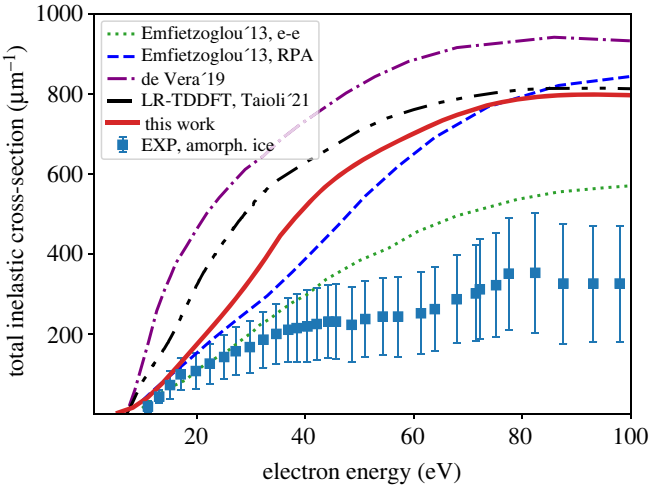

Figure 5. Total inelastic scattering cross section (equation (2.20)) as a function of the electron incident kinetic energy compared to experimental data for amorphous ice (EXP, amorph. ice) [91] and calculations by Emfietzoglou *et al.* [51], de Vera *et al.* [92] and Taioli *et al.* [65] (the sum of the excitation and ionization cross sections presented in fig. 3 of [65]).

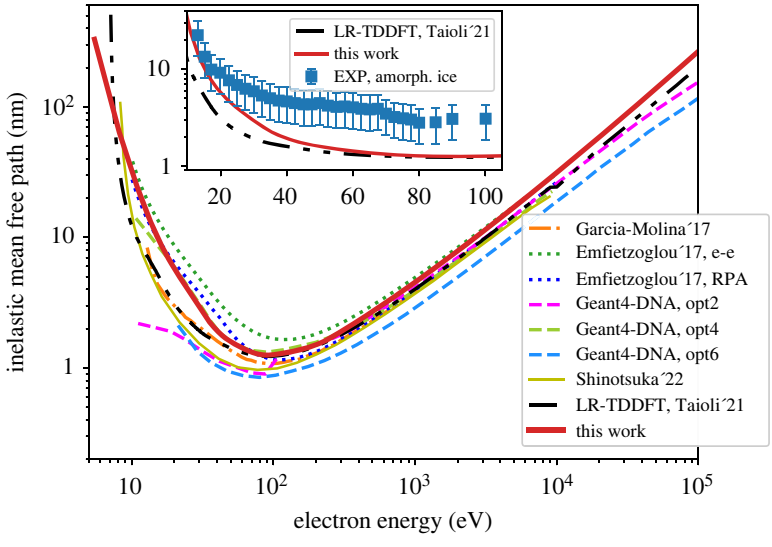

Figure 6. Inelastic mean free path as a function of the electron incident kinetic energy compared to calculations by Garcia-Molina *et al.* [47] (dash-dotted line), Emfietzoglou *et al.* [39] (dotted lines), Geant4-DNA options 2, 4 and 6 [23] (dashed lines), Shinotsuka *et al.* [93] and Taioli *et al.* [65] (dash-dot-dotted line, calculated as the inverse of the total cross section shown in figure 5). The inset shows the comparison of the LR-TDDFT results from this work and from Taioli *et al.* [65] with experimental data for amorphous ice [91].

The IMFP obtained in this work is shown in figure 6 and compared to the semi-empirical calculations [39,47], to the LR-TDDFT results from Taioli *et al.* [65], and to three Geant4-DNA constructors (the default, the Ioannina and the CPA100 models, denoted as opt2, opt4 and opt6) [23]. A more recent semi-empirical result of Shinotsuka *et al.* [93] obtained using the relativistic full Penn algorithm that includes the correction of the bandgap effect in water is also shown in figure 6. Our results quantitatively agree with the RPA model of Emfietzoglou *et al.* [39] in the whole energy range and with the IMFP obtained by Taioli *et al.* [65] at intermediate energies (from 100 eV to 10 keV). The data of Shinotsuka *et al.* [93] are below our IMFP and resemble more the shape of the results of Taioli *et al.* [65], except for the region around the minimum. The inset of figure 6 shows the comparison of the LR-TDDFT results from this work and from Taioli *et al.* [65] with the experimental data for amorphous ice below 100 eV. Both calculated results agree well at energies above 50 eV. Below this energy, the results of this work are closer to the experimental data than the ones from Taioli *et al.* [65].

Downloaded from https://royalsocietypublishing.org/ on 12 July 2022

In the Geant4-DNA default option (opt2), the total and inelastic cross sections for weakly bound electrons are calculated from the energy- and momentum-dependent complex dielectric function within the first Born approximation. In particular, the optical data model of Emfietzoglou *et al.* [94,95] is used, where the frequency dependence of the dielectric function at $q = 0$ is obtained by fitting experiments for both the real and imaginary part of the dielectric function, using a superposition of Drude-type functions with adjustable coefficients. A partitioning of the ELF to the electronic absorption channels at $q = 0$, proportional to the optical oscillator strength, enables the calculation of the cross sections for each individual excitation and ionization channel. The extension to the whole Bethe surface is made by semi-empirical dispersion relations for the Drude coefficients. Below a few hundred eV, where the first Born approximation is not applicable, a kinematic Coulomb-field correction and Mott-like XC terms are used [95]. For ionization of the O K-shell, total and differential cross sections are calculated analytically using the binary-encounter-approximation with exchange model (BEAX), an atomic model which depends only on the mean kinetic energy, the binding energy, the occupation number of the electrons, and where the deflection angle is determined from the kinematics of the binary collision, thus referring to sole vapour data.

In the Ioannina model [96,97], two problems appear in the default option, e.g. a brute-force truncation of the Drude function violating the *f*-sum rule and the consequent complexity in deriving $\epsilon_R(E, q)$ from $\epsilon_I(E, q)$ via Kramers–Kronig relations [23] are overcome via an algorithm which redistributes $\epsilon_I(E, q = 0)$ to the individual inelastic channels in a *f*-sum rule constrained and physically motivated manner. Below a few hundred eV, more accurate ionization cross sections, especially at energies near the binding energy, are obtained via methodological improvements of the Coulomb and Mott corrections. In the CPA100 models [98], excitation cross sections are calculated in the first Born approximation using the optical data model by Dingfelder *et al.* [33], which is also based on a Drude-function representation of $\epsilon(E, q)$ but uses a different parametrization. The ionization cross sections are calculated via the binary-encounter-Bethe (BEB) atomic model.

As no international recommendations exist yet for the mean free path, the only conclusion we can draw from the comparison between our results and the Geant4-DNA (figure 6) is that our first-principles result seems to well reproduce the Geant4-DNA opt4 at energies up to 1 keV. Above this energy, our result is slightly higher than opt2, opt4 and opt6. For the whole energy range, the IMFP from opt6 appears to be the lowest because of the larger inelastic cross sections in the 10 eV–10 keV range, as a consequence of using an atomic ionization model with the absence of screening [23]. The curve for opt2 shifts suddenly, through a clearly visible step, below 200 eV because of the activation of vibrational excitations, which reduce additional energy losses and thus reduce the IMFP. In opt4, excitations are strongly enhanced compared to ionization, the latter decreasing only moderately, which results in higher *W* values (the average energy to produce an ion pair) and smaller penetration distances [96]. Since XC effects mostly affect the results for $q \neq 0$, it is expected that XC corrections to the RPA will mostly influence the IMFP at low energies, where large-angle scattering collisions ($q \neq 0$) become important [39,51]. Indeed, as the comparison in the inset of figure 6 shows, the RPA result of this work differs from the AGGA results of Taioli *et al.* [65] only at energies below 50 eV. However, the inclusion of exchange and correlation does not improve the RPA result with respect to the experimental data.

The stopping power from LR-TDDFT is shown in figure 7 in comparison with the semi-empirical calculation [34,47], three Geant4-DNA options, and data from ICRU and ESTAR. As was the case for IMFP, our result is closer to opt4, until a few hundreds of eV, while at higher energies our stopping power is considerably smaller than the rest of the data presented. However, our stopping recovers the correct limit at the highest energies (10–100 MeV).

4.3. Analysis of different contributions to the electron energy loss function

Following the partition method described in §2.2, we calculated the ELF separated on contributions from different species, angular momenta and atomic pairs.

Figure 8*a* shows the contribution of orbital angular momenta *s*, *p* and *d* of all the atoms to the total ELF. Clearly, *p*-orbitals play a major role in forming the slopes of the ELF with a smaller contribution from *s*-orbitals. The maximum of the total ELF comes from a complicated interplay between the *s*- and *p*-levels, for which the ELF oscillates in an incoherent way. The results are validated by summing up all the contributions which add up to the total ELF.

Figure 8*b* shows the contribution of all the oxygen atoms and all the hydrogen atoms to the total ELF. Below the maximum, the total ELF mostly comes from the hydrogen atoms. At the maximum, hydrogen

Downloaded from https://royalsocietypublishing.org/ on 12 July 2022

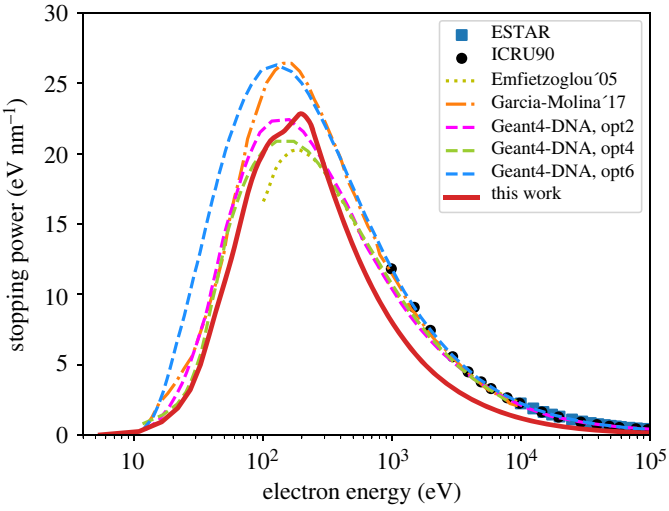

Figure 7. Electronic stopping power (equation (2.21)) as a function of the electron kinetic energy. Our results are compared to ESTAR [99] and ICRU90 [100] data, as well as calculations by Emfietzoglou *et al.* [34] (dotted line), Garcia-Molina *et al.* [47] (dash-dotted line) and Geant4-DNA options 2, 4 and 6 [23] (dashed lines).

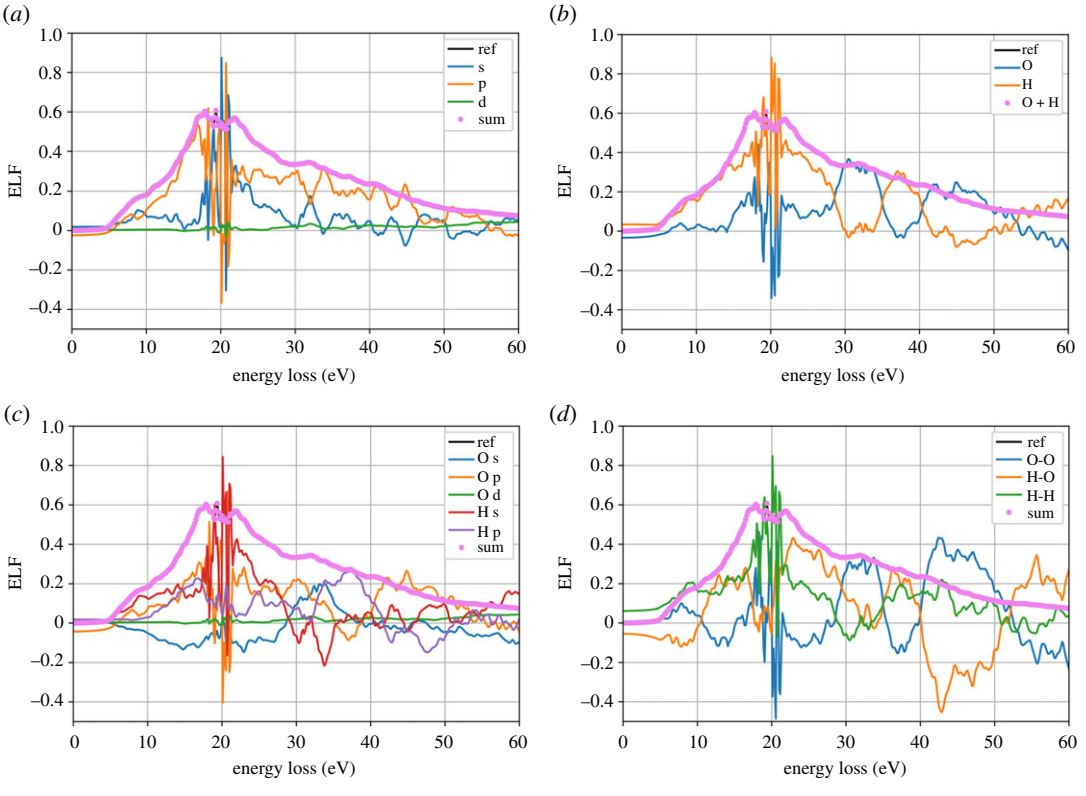

Figure 8. Contributions of (*a*) different angular momenta, (*b*) species, (*c*) angular momenta of different species and (*d*) pairs of species, to the total ELF ($q = 0.1$ a.u.) labelled as 'ref'.

atoms contribute more to the total ELF, while both curves again oscillate in opposite phases. Above the maximum, the two contributions oscillate resulting in a rather smooth total slope.

A detailed analysis, separating *s*, *p* and *d* orbitals of hydrogen and oxygen (figure 8*c*), shows that the main contribution to the ELF maximum is from the hydrogen *s*-levels and oxygen *p*-levels. Oxygen *s*-orbitals mostly contribute negatively. A significant contribution comes from the hydrogen *p*-orbital, indicating the excitation of the hydrogen electrons which populate the *p*-shell. Oxygen *d*-shell remains mostly unpopulated.

Downloaded from https://royalsocietypublishing.org/ on 12 July 2022

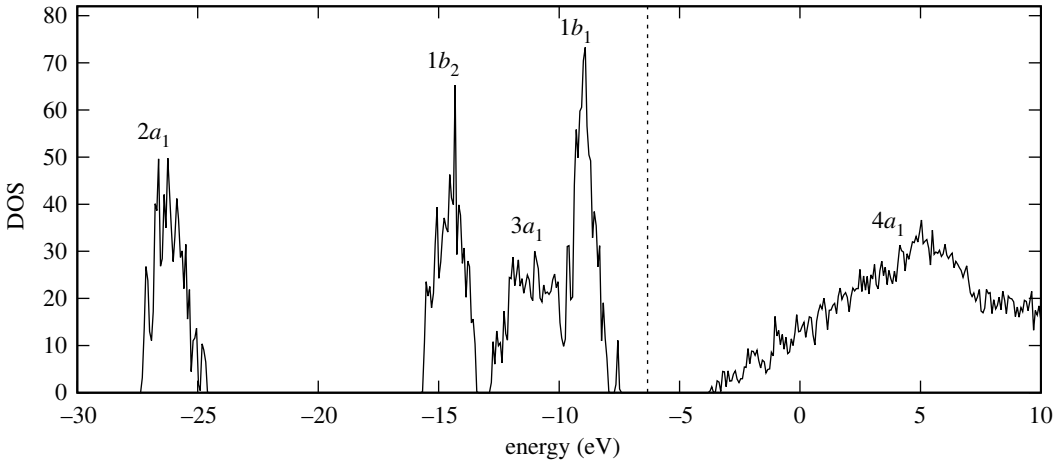

Figure 9. Electronic density of states of liquid water obtained within DFT. Vertical dashed line shows the Fermi level at −6.3 eV.

The contributions of species pairs are shown in figure 8*d*. Again, hydrogen plays the main role at low energy loss as H–H and H–O pairs. At the maximum of ELF, both H–O and O–O pairs contribute negatively to the total ELF. Similarly to the case of different species, there are incoherent oscillations in ELF above 25 eV for O–O and H–O pairs. However, in this case, the two contributions oscillate around zero cancelling each other. Thus, at high energy loss, the total ELF is mostly due to the H–H pairs.

4.4. Energy loss function and single-differential cross section for each molecular orbital

When constructing the Drude-type dielectric response function in semi-empirical methods, the continuum in the fitting procedure is usually represented by the outer shells of the water molecule [69,101]. Thus, the analysis of the ELF, and consequently the cross-sections, for each molecular orbital of water can be of interest for the MC track structure community for benchmarking of the semi-empirical models.

Here, we calculate the ELF for each occupied molecular orbital of the water molecule, i.e. the orbitals $2a_1$, $1b_2$, $3a_1$ and $1b_1$ [102]. In liquid water, the bands of crystal orbitals correspond to different symmetries of an isolated molecule. The bands can be seen in the electronic density of states (DOS) of liquid water sample shown in figure 9 as a function of energy which we calculated using the DFT implementation of the SIESTA code [77]. The binding energies of the four occupied orbitals of water are known from photoemission experiments. For liquid water, the binding energies are 30.90 eV for $2a_1$, 17.34 eV for $1b_2$, 13.50 eV for $3a_1$ and 11.16 eV for $1b_1$ [103]. Our results are slightly higher than experimental data, which is expected from the DFT method. However, our DOS is in good agreement with other DFT calculations [104].

Each feature in the DOS (figure 9) is labelled with the symmetry group corresponding to the isolated molecule. The DOS includes four outer occupied bands with symmetries $2a_1$, $1b_2$, $3a_1$ and $1b_1$ and one unoccupied band with the symmetry $4a_1$. For the ELF calculations, we only considered the occupied orbitals, i.e. the ones located below the Fermi level.

Since we cannot directly obtain the ELF for each molecular orbital from LR-TDDFT calculations, we sum up the values of ELF for all occupied crystal orbitals within the energy window corresponding to each symmetry. Figure 10 shows the contributions of occupied states to the total ELF resolved in energy in the optical limit for four selected values of the energy loss $E = 10.05$, 17.85, 22.05 and 31.95 eV, corresponding to the regions below, around and above the maximum of ELF (figure 3*a*). One can clearly distinguish four energy windows in which the ELF has non-zero values that can be directly correlated with the DOS (figure 9). Thus, summing up the ELF of each crystal orbital in each of the energy windows, we obtained the ELF for four molecular orbitals of water.

We repeated the calculations described above for the same values of the momentum transfer q as in figure 2 to obtain the partitioned ELF in the whole Bethe surface (E, q). This allowed us to compute the cross sections corresponding to each molecular orbital using equation (2.19). As an example, figure 11 shows the SDCS for the incident electron with kinetic energies $T = 100$ eV and 500 eV in water sample with 16 molecules. Each molecular orbital is observed to be responsible for a certain feature in the

Downloaded from https://royalsocietypublishing.org/ on 12 July 2022

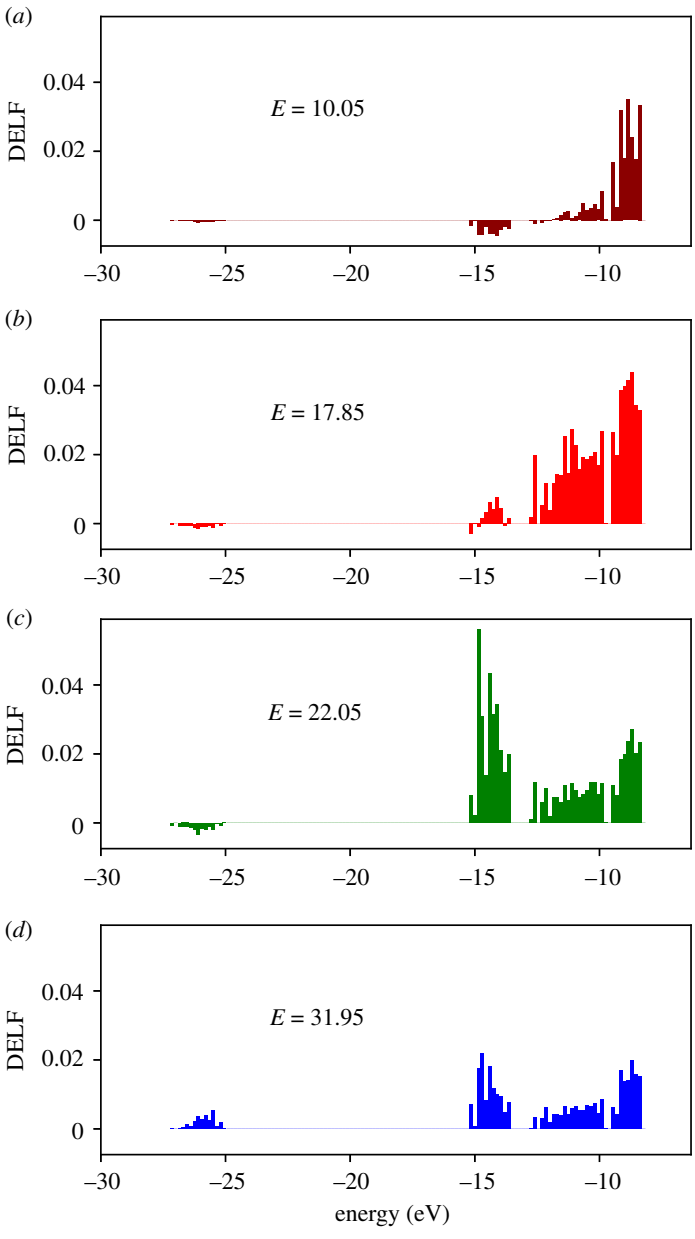

Figure 10. Contributions of different occupied states to the total ELF ($q = 0.1$) resolved in energy shown on panels (*a–d*) for the energy loss E values 10.05, 17.85, 22.05 and 31.95 eV, respectively.

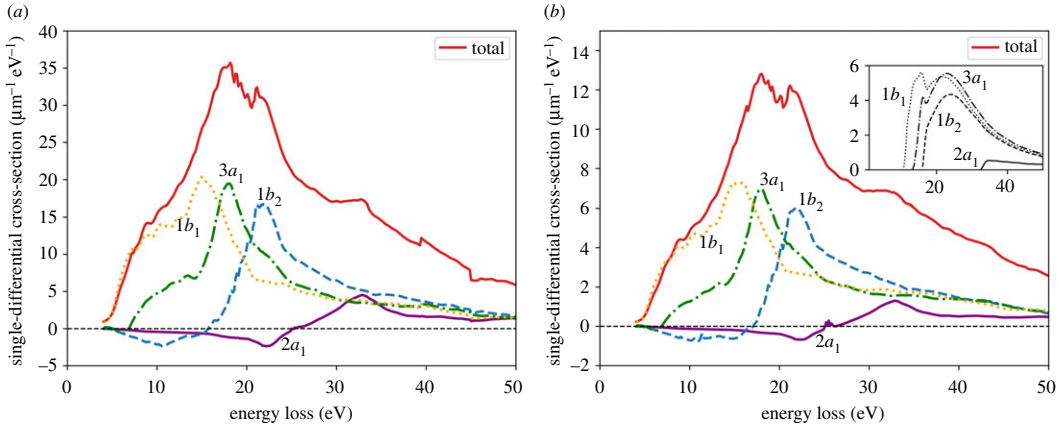

Figure 11. Single-differential cross section for each symmetry of a water molecule. Incident electron kinetic energy is (*a*) $T = 100$ eV and (*b*) $T = 500$ eV. The inset in (*b*) shows the results from [33].

Downloaded from https://royalsocietypublishing.org/ on 12 July 2022

total SDCS. The partitioning also looks very similar at both electron incident energies. The cross section for energy losses below 10 eV is almost entirely due to the contribution from the highest occupied molecular orbital (HOMO) $1b_1$. Deeper shells contribute at higher energy losses. The orbital $2a_1$ has a minor contribution only at high energy losses. The observed behaviour is in a qualitative agreement with available data from the dielectric formalism within the first Born approximation [33,69] (see inset to figure 11*b*).

5. Conclusion

In summary, in this work, we computed several quantities important for the description of inelastic scattering of electrons in liquid water using a linear-response formulation of TDDFT. A good agreement with experimental data was obtained for ELF in the optical limit as well as at finite values of the momentum transfer. We thoroughly tested our results for dependence on the system size and the choice of the DFT parameters.

Additionally, we provided a detailed analysis of the ELF in the optical limit in terms of contributions from different species, species pairs and orbital angular momenta.

Furthermore, we computed the SDCS, total inelastic cross section, IMFP and the electronic stopping power from the ELF. Our results are in a good agreement with the semi-empirical calculations. Thus, LR-TDDFT offers an alternative method to the standard semi-empirical calculations and provides useful input for more detailed MC-TS simulations. It is envisioned that the investigated quantities have the potential to be of direct use in open source TS codes like Geant4-DNA. In particular, the decomposition of the cross sections on different molecular orbital channels, calculated *ab initio* for the first time in this work, can be used as a benchmarking for semi-empirical models.

Ethics. The authors declare that this paper conforms to the ethical code of the Royal Society.

Data accessibility. Data files with the IMFP, the electronic stopping power and the SDCS for kinetic energies of 100 eV, 500 eV, 1 keV and 5 keV are provided in the Dryad Digital Repository: https://doi.org/10.5061/dryad.d51c5b057 [108].

Authors' contributions. N.E.K.: conceptualization, formal analysis, investigation, methodology, validation, visualization, writing—original draft; P.K.: methodology, software, supervision, writing—original draft, writing—review and editing; F.D.P.: conceptualization, funding acquisition, project administration, supervision, validation, writing—original draft, writing—review and editing; J.K.: conceptualization, funding acquisition, methodology, supervision, writing—review and editing; E.A.: conceptualization, funding acquisition, supervision, validation, writing—review and editing; D.E.: methodology, validation, writing—review and editing.

All authors gave final approval for publication and agreed to be held accountable for the work performed therein.

Conflict of interest declaration. The authors have no competing interests.

Funding. The presented work has been funded by the Research Executive Agency under the European Union's Horizon 2020 Research and Innovation programme (project ESC2RAD: Enabling Smart Computations to study space RADiation effects, grant agreement no. 776410). J.K. was supported by the Beatriz Galindo Program (BEAGAL18/00130) from the Ministerio de Educación y Formación Profesional of Spain, and by the Comunidad de Madrid through the Convenio Plurianual with Universidad Politécnica de Madrid in its line of action Apoyo a la realización de proyectos de I + D para investigadores Beatriz Galindo, within the framework of V PRICIT (V Plan Regional de Investigación Científica e Innovación Tecnológica). E.A. acknowledges the funding from Spanish MINECO through grant no. FIS2015-64886-C5-1-P, and from Spanish MICIN through grant no. PID2019-107338RB-C61/AEI/10.13039/501100011033, as well as a María de Maeztu award to Nanogune, grant no. CEX2020-001038-M funded by MCIN/AEI/10.13039/501100011033.

Acknowledgements. We thank Simone Taioli and Pablo de Vera for providing us with the data related to their recent publications. We are grateful for computational resources provided by Donostia International Physics Center (DIPC) Computer Center and Barcelona Supercomputer Center. We thank Dr Daniel Muñoz Santiburcio for providing the water structures obtained by CP2K calculations.

Appendix A. Test results and additional data for single-differential cross section

To check the convergence of our results with respect to the particular configuration of the water molecules in the sample, we have calculated the ELF for several different samples. One of the samples with the initial configuration of PBE-64 was equilibrated with the van der Waals (DRSLL) [105,106] XC functional in the BOMD simulation. Three snapshots were chosen, after 2.7 ps, 5.0 ps and 6.8 ps of the BOMD, denoted with subscripts VdW-64_1,2,3 to test the convergence of the LR-TDDFT results with the sample configuration. The sample RPBE-64 (RPBE-128) contains 64 (128) molecules in a cubic

Downloaded from https://royalsocietypublishing.org/ on 12 July 2022

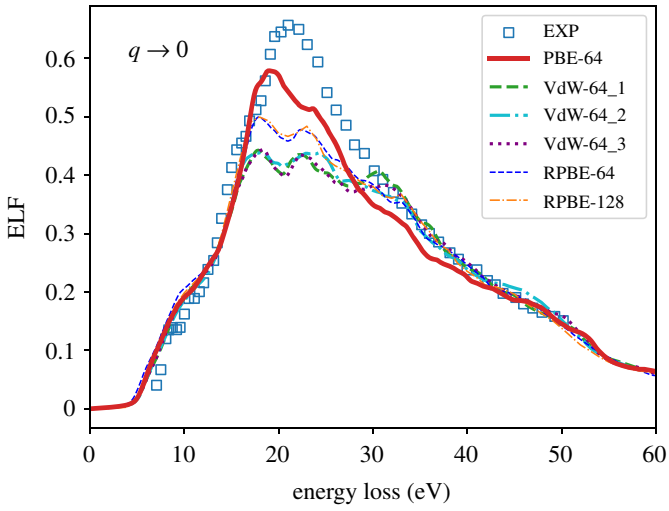

Figure 12. ELF of liquid water in the optical limit ($q \to 0$) as a function of energy loss (eV) calculated with LR-TDDFT for different water structures (see text for details) with the broadening constant $\eta = 0.3$ eV and the momentum transfer $q = 0.1$ a.u. The DZP basis set with an energy shift of 20 meV is used in the SIESTA calculations. IXS data ($q = 0$) is from Hayashi *et al.* [36].

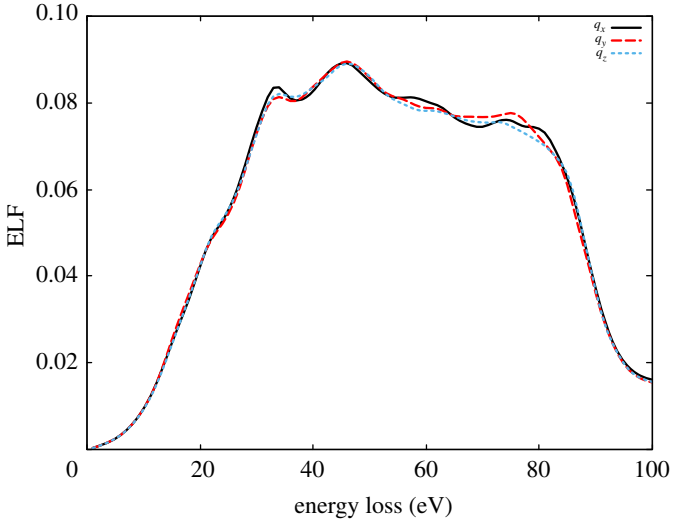

Figure 13. ELF of liquid water (sample PBE-64) for $q = 1.5$ a.u. as a function of energy loss (eV) calculated with LR-TDDFT for different directions of the momentum transfer: q_x, q_y and q_z.

unit cell with the lattice constant $a = 12.43$ (15.66) Å to correspond to the experimental water density at 300 K and 1 bar. The SCF convergence threshold during the MD was st to 2×10^{-7}. The equilibration was performed with BOMD of the CP2K code [107], with RPBE-D3 XC functional and a TZV2P basis set at 300 K in the NVT ensemble (Nosé-Hoover-chains thermostat) for 10 ps. A larger sample with 128 molecules was used to test the dependence of our results on the system size.

The tests have shown that the ELF is similar for all the structures and that it does not depend on the system size or a particular snapshot configuration among the ones generated as described, once properly equilibrated (figure 12). The three different VdW snapshots give practically the same results. The same is true for both RPBE samples, with 64 and 128 molecules, the use of which leads to the same results for the ELF. Overall, the tests show that the ELF depends on neither the size of the sample used in the calculations, nor the exact configuration of the water molecules in the sample. The choice of the XC functional, however, affects the ELF results in the peak area, with the PBE functional giving the closest result to the experimental data. For this reason, we chose to perform all the calculations for the cross sections and stopping power using the ELF obtained with the PBE-64 structure.

Downloaded from https://royalsocietypublishing.org/ on 12 July 2022

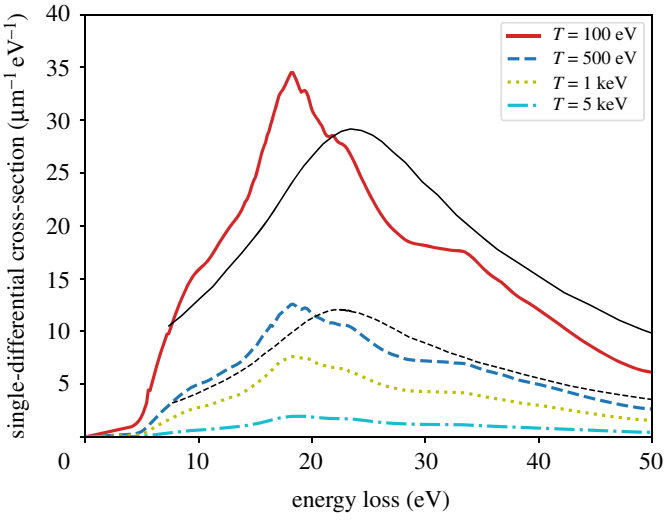

Figure 14. The SDCS for the electron kinetic energies of 100 eV, 500 eV, 1 keV and 5 keV as a function of energy loss. Thin black lines show the RPA results from Emfietzoglou *et al.* [51] for electron energies of 100 eV (solid black line) and 500 eV (dashed black line).

The use of the scalar value of the momentum transfer is justified by the fact that the ELF is isotropic, i.e. it is very similar for all the directions of the momentum transfer vector, as can be seen in figure 13.

Figure 14 presents the SDCS for incident electron kinetic energies of 100 eV, 500 eV, 1 keV and 5 keV compared to available results from Emfietzoglou *et al.* [51] for energies of 100 and 500 eV.

References

1. Plante I, Cucinotta FA. 2009 Cross sections for the interactions of 1 eV–100 MeV electrons in liquid water and application to Monte-Carlo simulation of HZE radiation tracks. *New J. Phys.* **11**, 063047. (doi:10.1088/1367-2630/11/6/063047)
2. Pimblott SM, LaVerne JA. 2007 Production of low-energy electrons by ionizing radiation. *Radiat. Phys. Chem.* **76**, 1244–1247. (doi:10.1016/j.radphyschem.2007.02.012)
3. Michaud M, Wen ASL. 2003 Cross sections for low-energy (1–100 eV) electron elastic and inelastic scattering in amorphous ice. *Radiat. Res.* **159**, 3–22. (doi:10.1667/0033-7587(2003)159[0003:CSFLEE]2.0.CO;2)
4. Boudaïffa B, Cloutier P, Hunting D, Huels MA, Sanche L. 2000 Resonant formation of DNA strand breaks by low-energy (3 to 20 eV) electrons. *Science* **287**, 1658–1660. (doi:10.1126/science.287.5458.1658)
5. Alizadeh E, Orlando TM, Sanche L. 2015 Biomolecular damage induced by ionizing radiation: the direct and indirect effects of low-energy electrons on DNA. *Annu. Rev. Phys. Chem.* **66**, 379–398. (doi:PMID:25580626)
6. Khorsandgolchin G, Sanche L, Cloutier P, Wagner JR. 2019 Strand breaks induced by very low energy electrons: product analysis and mechanistic insight into the reaction with TpT. *J. Am. Chem. Soc.* **141**, 10315–10323. (doi:10.1021/jacs.9b03295)
7. Surdutovich E, Solov'yov A. 2014 Multiscale approach to the physics of radiation damage with ions. *Eur. Phys. J. D* **68**, 353. (doi:10.1140/epjd/e2014-50004-0)
8. Denifl S, Märk TD, Scheier P. 2012 The role of secondary electrons in radiation damage. In *Radiation damage in biomolecular systems* (eds G García Gómez-Tejedor, MC Fuss), pp. 45–58. Dordrecht, The Netherlands: Springer.
9. Nikjoo H, Goodhead DT. 1991 Track structure analysis illustrating the prominent role of low-energy electrons in radiobiological effects of low-LET radiations. *Phys. Med. Biol.* **36**, 229–38. (doi:10.1088/0031-9155/36/2/007)
10. Nikjoo HLL. 2010 RBE of low energy electrons and photons. *Phys. Med. Biol.* **55**, R65–109. (doi:10.1088/0031-9155/55/10/R01)
11. Rabus H, Nettelbeck H. 2011 Nanodosimetry: bridging the gap to radiation biophysics. *Radiat. Meas.* **46**, 1522–1528. (doi:10.1016/j.radmeas.2011.02.009)
12. Huels MA, Boudaïffa B, Cloutier P, Hunting D, Sanche L. 2003 Single, double, and multiple double strand breaks induced in DNA by 3–100 eV electrons. *J. Am. Chem. Soc.* **125**, 4467–4477. (doi:10.1021/ja029527x)
13. Prise KM, Folkard M, Michael BD, Vojnovic B, Brocklehurst B, Hopkirk A, Munro IH. 2000 Critical energies for SSB and DSB induction in plasmid DNA by low-energy photons: action spectra for strand-break induction in plasmid DNA irradiated in vacuum. *Int. J. Radiat. Biol.* **76**, 881–890. (doi:10.1080/09553000050050891)
14. Kohanoff J, McAllister M, Tribello GA, Gu B. 2017 Interactions between low energy electrons and DNA: a perspective from first-principles simulations. *J. Phys.: Condens. Matter* **29**, 383001. (doi:10.1088/1361-648X/aa79e3)
15. Nikjoo H, Uehara S, Emfietzoglou D, Cucinotta F. 2006 Track-structure codes in radiation research. *Radiat. Meas.* **41**, 1052–1074. (doi:10.1016/j.radmeas.2006.02.001)
16. Nikjoo H, Emfietzoglou D, Liamsuwan T, Taleei R, Liljequist D, Uehara S. 2016 Radiation track, DNA damage and response: a review. *Rep. Prog. Phys.* **79**, 116601. (doi:10.1088/0034-4885/79/11/116601)
17. Dingfelder M. 2012 Track-structure simulations for charged particles. *Health Phys.* **103**, 590–595. (doi:10.1097/HP.0b013e3182621292)
18. Chatzipapas KP, Papadimitroulas P, Emfietzoglou D, Kalospyros SA, Hada M, Georgakilas AG, Kagadis GC. 2020 Ionizing radiation and complex DNA damage: quantifying the radiobiological damage using Monte Carlo simulations. *Cancers* **12**, 799. (doi:10.3390/cancers12040799)
19. Semenenko V, Turner J, Borak T. 2003 NOREC, a Monte Carlo code for simulating electron tracks in liquid water. *Radiat. Environ. Biophys.* **42**, 213–217. (doi:10.1007/s00411-003-0201-z)
20. Liamsuwan T, Emfietzoglou D, Uehara S, Nikjoo H. 2012 Microdosimetry of low-energy electrons. *Int. J. Radiat. Biol.* **88**, 899–907. (doi:10.3109/09553002.2012.699136)
21. Paretzke H. 1987 Radiation track structure theory. In *Kinetics of non-homogeneous processes* (ed. GR Freeman), pp. 89–170. New York, NY: Wiley.
22. Plante I, Cucinotta FA. 2008 Ionization and excitation cross sections for the interaction of HZE particles in liquid water and application to

Downloaded from https://royalsocietypublishing.org/ on 12 July 2022

Monte Carlo simulation of radiation tracks. *New J. Phys.* **10**, 125020. (doi:10.1088/1367-2630/10/12/125020)

23. Incerti S *et al.* 2018 Geant4-DNA example applications for track structure simulations in liquid water: a report from the Geant4-DNA Project. *Med. Phys.* **45**, e722–e739. (doi:10.1002/mp.13048)
24. Bernal MA *et al.* 2015 Track structure modeling in liquid water: a review of the Geant4-DNA very low energy extension of the Geant4 Monte Carlo simulation toolkit. *Phys. Med.* **31**, 861–874. (doi:10.1016/j.ejmp.2015.10.087)
25. Garty G *et al.* 2010 A nanodosimetric model of radiation-induced clustered DNA damage yields. *Phys. Med. Biol.* **55**, 761–781. (doi:10.1088/0031-9155/55/3/015)
26. Champion C. 2013 Quantum-mechanical predictions of electron-induced ionization cross sections of DNA components. *J. Chem. Phys.* **138**, 184306. (doi:10.1063/1.4802962)
27. Plante I, Cucinotta FA. 2015 Binary-Encounter-Bethe ionisation cross sections for simulation of DNA damage by the direct effect of ionising radiation. *Radiat. Prot. Dosim.* **166**, 19–23. (doi:10.1093/rpd/ncv143)
28. Margis S, Magouni M, Kyriakou I, Georgakilas AG, Incerti S, Emfietzoglou D. 2020 Microdosimetric calculations of the direct DNA damage induced by low energy electrons using the Geant4-DNA Monte Carlo code. *Phys. Med. Biol.* **65**, 045007. (doi:10.1088/1361-6560/ab6b47)
29. de Vera P, Abril I, Garcia-Molina R. 2021 Excitation and ionisation cross-sections in condensed-phase biomaterials by electrons down to very low energy: application to liquid water and genetic building blocks. *Phys. Chem. Chem. Phys.* **23**, 5079–5095. (doi:10.1039/D0CP04951D)
30. Ritchie RH, Howie A. 1977 Electron excitation and the optical potential in electron microscopy. *Phil. Mag.* **36**, 463–481. (10.1080/14786437708244948)
31. Ritchie RH, Hamm RN, Turner JE, Wright HA, Bolch WE. 1991 *Physical and chemical mechanisms in molecular radiation biology*. Boston, MA: Springer.
32. Penn DR. 1987 Electron mean-free-path calculations using a model dielectric function. *Phys. Rev. B* **35**, 482–486. (doi:10.1103/PhysRevB.35.482)
33. Dingfelder M, Hantke D, Inokuti M, Paretzke HG. 1999 Electron inelastic-scattering cross sections in liquid water. *Radiat. Phys. Chem.* **53**, 1–18. (doi:10.1016/S0969-806X(97)00317-4)
34. Emfietzoglou D, Cucinotta FA, Nikjoo H. 2005 A complete dielectric response model for liquid water: a solution of the Bethe Ridge problem. *Radiat. Res.* **164**, 202. (doi:10.1667/RR3399)
35. Watanabe N, Hayashi H, Udagawa Y. 1997 Bethe surface of liquid water determined by inelastic X-ray scattering spectroscopy and electron correlation effects. *Bull. Chem. Soc. Jpn.* **70**, 719–726. (doi:10.1246/bcsj.70.719)
36. Hayashi H, Watanabe N, Udagawa Y, Kao CC. 2000 The complete optical spectrum of liquid water measured by inelastic X-ray scattering. *Proc. Natl Acad. Sci. USA* **97**, 6264–6266. (doi:10.1073/pnas.110572097)
37. Abril I, Garcia-Molina R, Denton CD, Pérez-Pérez FJ, Arista NR. 1998 Dielectric description of wakes and stopping powers in solids. *Phys. Rev. A* **58**, 357–366. (doi:10.1103/PhysRevA.58.357)
38. Inokuti M. 1971 Inelastic collisions of fast charged particles with atoms and molecules—the Bethe theory revisited. *Rev. Mod. Phys.* **43**, 297–347. (doi:10.1103/RevModPhys.43.297)
39. Emfietzoglou D, Kyriakou I, Garcia-Molina R, Abril I. 2017 Inelastic mean free path of low-energy electrons in condensed media: beyond the standard models. *Surf. Interface Anal.* **49**, 4–10. (doi:10.1002/sia.5878)
40. Nikjoo H, Uehara S. 1994 Comparison of various Monte Carlo track structure codes for energetic electrons in gaseous and liquid water. In *Computational approaches in molecular radiation biology: Monte Carlo methods* (eds MN Varma, A Chaterjee), pp. 167–185. Boston, MA: Springer.
41. Emfietzoglou D, Kyriakou I, Abril I, Garcia-Molina R, Nikjoo H. 2012 Inelastic scattering of low-energy electrons in liquid water computed from optical-data models of the Bethe surface. *Int. J. Radiat. Biol.* **88**, 22–28. (doi:10.3109/09553002.2011.588061)
42. Villagrasa C *et al.* 2018 Assessing the contribution of cross-sections to the uncertainty of Monte Carlo calculations in micro- and nanodosimetry. *Radiat. Prot. Dosim.* **183**, 11–16. (doi:10.1093/rpd/ncy240)
43. Lampe N, Karamitros M, Breton V, Brown JMC, Kyriakou I, Sakata D, Sarramia D, Incerti S. 2018 Mechanistic DNA damage simulations in Geant4-DNA part 1: a parameter study in a simplified geometry. *Phys. Med.* **48**, 135–145. (doi:10.1016/j.ejmp.2018.02.011)
44. Champion C. 2003 Theoretical cross sections for electron collisions in water: structure of electron tracks. *Phys. Med. Biol.* **48**, 2147–2168. (doi:10.1088/0031-9155/48/14/308)
45. Dingfelder M. 2007 Track structure: time evolution from physics to chemistry. *Radiat. Prot. Dosim.* **122**, 16–21. (doi:10.1093/rpd/ncl494)
46. Emfietzoglou D, Papamichael G, Nikjoo H. 2017 Monte Carlo electron track structure calculations in liquid water using a new model dielectric response function. *Radiat. Res.* **188**, 355–368. (doi:10.1667/RR14705.1)
47. Garcia-Molina R, Abril I, Kyriakou I, Emfietzoglou D. 2017 Inelastic scattering and energy loss of swift electron beams in biologically relevant materials. *Surf. Interface Anal.* **49**, 11–17. (doi:10.1002/sia.5947)
48. Friedland W, Dingfelder M, Kundrát P, Jacob P. 2011 Track structures, DNA targets and radiation effects in the biophysical Monte Carlo simulation code PARTRAC. *Mutat. Res./Fundam. Mol. Mech. Mutagen.* **711**, 28–40. (doi:10.1016/j.mrfmmm.2011.01.003)
49. Taleei R, Nikjoo H. 2012 Repair of the double-strand breaks induced by low energy electrons: a modelling approach. *Int. J. Radiat. Biol.* **88**, 948–953. (doi:10.3109/09553002.2012.695098)
50. Bug MU, Yong Baek W, Rabus H, Villagrasa C, Meylan S, Rosenfeld AB. 2017 An electron-impact cross section data set (10 eV–1 keV) of DNA constituents based on consistent experimental data: a requisite for Monte Carlo simulations. *Radiat. Phys. Chem.* **130**, 459–479. (doi:10.1016/j.radphyschem.2016.09.027)
51. Emfietzoglou D, Kyriakou I, Garcia-Molina R, Abril I, Nikjoo H. 2013 Inelastic cross sections for low-energy electrons in liquid water: exchange and correlation effects. *Radiat. Res.* **180**, 499–513. (doi:10.1667/RR13362.1)
52. Emfietzoglou D, Nikjoo H, Pathak A. 2006 A comparative study of dielectric response function models for liquid water. *Radiat. Prot. Dosim.* **122**, 61–65. (doi:10.1093/rpd/ncl414)
53. Nguyen-Truong HT. 2018 Low-energy electron inelastic mean free paths for liquid water. *J. Phys. Condens. Matter* **30**, 155101. (doi:10.1088/1361-648X/aab40a)
54. Quinto MA, Monti JM, Weck PF, Fojón OA, Hanssen J, Rivarola RD, Senot P, Champion C. 2017 Monte Carlo simulation of proton track structure in biological matter. *Eur. Phys. J. D* **71**, 130. (doi:10.1140/epjd/e2017-70709-6)
55. Verkhovtsev A, Traore A, Muñoz A, Blanco F, García G. 2017 Modeling secondary particle tracks generated by intermediate- and low-energy protons in water with the low-energy particle track simulation code. *Radiat. Phys. Chem.* **130**, 371–378. (doi:10.1016/j.radphyschem.2016.09.021)
56. Signorell R. 2020 Electron scattering in liquid water and amorphous ice: a striking resemblance. *Phys. Rev. Lett.* **124**, 205501. (doi:10.1103/PhysRevLett.124.205501)
57. Zein SA, Bordage MC, Francis Z, Macetti G, Genoni A, Dal Cappello C, Shin WG, Incerti S. 2021 Electron transport in DNA bases: an extension of the Geant4-DNA Monte Carlo toolkit. *Nucl. Instrum. Methods Phys. Res. B* **488**, 70–82. (doi:10.1016/j.nimb.2020.11.021)
58. Costa F *et al.* 2020 A complete cross section data set for electron scattering by pyridine: modelling electron transport in the energy range 0–100 eV. *Int. J. Mol. Sci.* **21**, 6947. (doi:10.3390/ijms21186947)
59. Runge E, Gross EKU. 1984 Density-functional theory for time-dependent systems. *Phys. Rev. Lett.* **52**, 997–1000. (doi:10.1103/PhysRevLett.52.997)
60. Marques MAL, Maitra N, Nogueira FMS, Gross EKU, Rubio A. 2012 *Fundamentals of time-dependent density functional theory*. Berlin, Germany: Springer.
61. Ullrich CA. 2012 *Time-dependent density-functional theory: concepts and applications*. Oxford, UK: Oxford University Press.
62. Yabana K, Bertsch GF. 1996 Time-dependent local-density approximation in real time. *Phys. Rev. B* **54**, 4484–4487. (doi:10.1103/PhysRevB.54.4484)
63. Yabana K, Bertsch GF. 1999 Time-dependent local-density approximation in real time: application to conjugated molecules. *Int. J. Quantum Chem.* **75**, 55–66. (doi:10.1002/(SICI)1097-461X(1999)75:1<55::AID-QUA6>3.0.CO;2-K)
64. Tavernelli I. 2006 Electronic density response of liquid water using time-dependent density

Downloaded from https://royalsocietypublishing.org/ on 12 July 2022

functional theory. *Phys. Rev. B* **73**, 094204. (doi:10.1103/PhysRevB.73.094204)

65. Taioli S, Trevisanutto PE, de Vera P, Simonucci S, Abril I, Garcia-Molina R, Dapor M. 2021 Relative role of physical mechanisms on complex biodamage induced by carbon irradiation. *J. Phys. Chem. Lett.* **12**, 487–493. (doi:10.1021/acs.jpclett.0c03250)
66. Koval P, Ljungberg MP, Foerster D, Sánchez-Portal D. 2015 Computation of electron energy loss spectra by an iterative method. *Nucl. Instrum. Methods Phys. Res. B* **354**, 216–219. (doi:10.1016/j.nimb.2014.11.080)
67. Foerster D, Koval P, Coulaud O, Sánchez-Portal D. 2008 MBPT_LCAO. See http://mbpt-domiprod.wikidot.com.
68. Ren X, Rinke P, Joas C, Scheffler M. 2012 Random-phase approximation and its applications in computational chemistry and materials science. *J. Mater. Sci.* **47**, 7447–7471. (doi:10.1007/s10853-012-6570-4)
69. Emfietzoglou D. 2003 Inelastic cross-sections for electron transport in liquid water: a comparison of dielectric models. *Radiat. Phys. Chem.* **66**, 373–385. (doi:10.1016/S0969-806X(02)00504-2)
70. Botti S, Schindlmayr A, Sole RD, Reining L. 2007 Time-dependent density-functional theory for extended systems. *Rep. Prog. Phys.* **70**, 357–407. (doi:10.1088/0034-4885/70/3/R02)
71. Wiser N. 1963 Dielectric constant with local field effects included. *Phys. Rev.* **129**, 62–69. (doi:10.1103/PhysRev.129.62)
72. Petersilka M, Gossmann UJ, Gross EKU. 1996 Excitation energies from time-dependent density-functional theory. *Phys. Rev. Lett.* **76**, 1212–1215. (doi:10.1103/PhysRevLett.76.1212)
73. Olsen T, Patrick CE, Bates JE, Ruzsinszky A, Thygesen KS. 2019 Beyond the RPA and GW methods with adiabatic xc-kernels for accurate ground state and quasiparticle energies. *npj Comput. Mater.* **5**, 106. (doi:10.1038/s41524-019-0242-8)
74. Adler SL. 1962 Quantum theory of the dielectric constant in real solids. *Phys. Rev.* **126**, 413–420. (doi:10.1103/PhysRev.126.413)
75. Artacho E. 2007 Electronic stopping in insulators: a simple model. *J. Phys.: Condens. Matter* **19**, 275211. (doi:10.1088/0953-8984/19/27/275211)
76. Lim A, Foulkes WMC, Horsfield AP, Mason DR, Schleife A, Draeger EW, Correa AA. 2016 Electron elevator: excitations across the band gap via a dynamical gap state. *Phys. Rev. Lett.* **116**, 043201. (doi:10.1103/PhysRevLett.116.043201)
77. Soler J, Artacho E, Gale J, García A, Junquera J, Ordejón P, Sánchez-Portal D. 2002 The SIESTA method for ab initio order-N materials simulation. *J. Phys. Condens. Matter* **14**, 2745. (doi:10.1088/0953-8984/14/11/302)
78. Monkhorst HJ, Pack JD. 1976 Special points for Brillouin-zone integrations. *Phys. Rev. B* **13**, 5188–5192. (doi:10.1103/PhysRevB.13.5188)
79. Ceperley DM, Alder BJ. 1980 Ground state of the electron gas by a stochastic method. *Phys. Rev. Lett.* **45**, 566–569. (doi:10.1103/PhysRevLett.45.566)
80. Troullier N, Martins JL. 1991 Efficient pseudopotentials for plane-wave calculations. *Phys. Rev. B* **43**, 1993–2006. (doi:10.1103/PhysRevB.43.1993)
81. Artacho E, Sánchez-Portal D, Ordejón P, García A, Soler JM. 1999 Linear-scaling ab-initio calculations for large and complex systems. *Phys. Status Solidi B* **215**, 809–817. (doi:10.1002/(SICI)1521-3951(199909)215:1<809::AID-PSSB809>3.0.CO;2-0)
82. Junquera J, Paz O, Sánchez-Portal D, Artacho E. 2001 Numerical atomic orbitals for linear-scaling calculations. *Phys. Rev. B* **64**, 235111. (doi:10.1103/PhysRevB.64.235111)
83. Perdew JP, Burke K, Ernzerhof M. 1996 Generalized gradient approximation made simple. *Phys. Rev. Lett.* **77**, 3865–3868. (doi:10.1103/PhysRevLett.77.3865)
84. Botti S. 2004 Applications of time-dependent density functional theory. *Phys. Scr.* **T109**, 54. (doi:10.1238/Physica.Topical.109a00054)
85. Gross EKU, Maitra NT. 2012 Introduction to TDDFT. In *Fundamentals of time-dependent density functional theory* (eds MAL Marques, NT Maitra, FMS Nogueira, EKU Gross, A Rubio), pp. 53–99. Berlin, Germany: Springer.
86. Ghosez P, Gonze X, Godby RW. 1997 Long-wavelength behavior of the exchange-correlation kernel in the Kohn-Sham theory of periodic systems. *Phys. Rev. B* **56**, 12811–12817. (doi:10.1103/PhysRevB.56.12811)
87. Kim YH, Görling A. 2002 Exact Kohn-Sham exchange kernel for insulators and its long-wavelength behavior. *Phys. Rev. B* **66**, 035114. (doi:10.1103/PhysRevB.66.035114)
88. Waidmann S, Knupfer M, Arnold B, Fink J, Fleszar A, Hanke W. 2000 Local-field effects and anisotropic plasmon dispersion in diamond. *Phys. Rev. B* **61**, 10 149–10 153. (doi:10.1103/PhysRevB.61.10149)
89. Olevano V, Reining L. 2001 Excitonic effects on the silicon plasmon resonance. *Phys. Rev. Lett.* **86**, 5962–5965. (doi:10.1103/PhysRevLett.86.5962)
90. Garcia-Molina R, Abril I, Heredia-Avalos S, Kyriakou I, Emfietzoglou D. 2011 A combined molecular dynamics and Monte Carlo simulation of the spatial distribution of energy deposition by proton beams in liquid water. *Phys. Med. Biol.* **56**, 6475–6493. (doi:10.1088/0031-9155/56/19/019)
91. Michaud M, Wen A, Sanche L. 2003 Cross sections for low-energy (1–100 eV) electron elastic and inelastic scattering in amorphous ice. *Radiat. Res.* **159**, 3–22. (doi:10.1667/0033-7587(2003)159[0003:CSFLEE]2.0.CO;2)
92. de Vera P, Garcia-Molina R. 2019 Electron inelastic mean free paths in condensed matter down to a few electronvolts. *J. Phys. Chem. C* **123**, 2075–2083. (doi:10.1021/acs.jpcc.8b10832)
93. Shinotsuka H, Tanuma S, Powell CJ. 2022 Calculations of electron inelastic mean free paths. XIII. Data for 14 organic compounds and water over the 50 eV to 200 keV range with the relativistic full Penn algorithm. *Surf. Interface Anal.* **54**, 534–560. (doi:10.1002/sia.7064)
94. Emfietzoglou D, Karava K, Papamichael G, Moscovitch M. 2003 Monte Carlo simulation of the energy loss of low-energy electrons in liquid water. *Phys. Med. Biol.* **48**, 2355–2371. (doi:10.1088/0031-9155/48/15/308)
95. Emfietzoglou D, Nikjoo H. 2005 The effect of model approximations on single-collision distributions of low-energy electrons in liquid water. *Radiat. Res.* **163**, 98–111. (doi:10.1667/RR3281)
96. Kyriakou I, Šefl M, Nourry V, Incerti S. 2016 The impact of new Geant4-DNA cross section models on electron track structure simulations in liquid water. *J. Appl. Phys.* **119**, 194902. (doi:10.1063/1.4950808)
97. Kyriakou I, Incerti S, Francis Z. 2015 Technical note: improvements in Geant4 energy-loss model and the effect on low-energy electron transport in liquid water. *Med. Phys.* **42**, 3870–3876. (doi:10.1118/1.4921613)
98. Bordage M, Bordes J, Edel S, Bardiés M, Lampe N, Incerti S. 2016 Implementation of new physics models for low energy electrons in liquid water in Geant4-DNA. *Phys. Med.: Eur. J. Med. Phys.* **32**, 1833–1840. (doi:10.1016/j.ejmp.2016.10.006)
99. Berger M, Coursey J, Zucker M. 1999 ESTAR, PSTAR, and ASTAR: computer programs for calculating stopping-power and range tables for electrons, protons, and helium ions (version 1.21). See http://physics.nist.gov/Star (accessed 27 April 2022).
100. Seltzer SM, Fernandez-Varea JM, Andreo P, Bergstrom PM, Burns DT, Krajcar Bronić I, Ross CK, Salvat F. 2016 *Key data for ionizing-radiation dosimetry: measurement standards and applications, ICRU Report 90*. Technical Report. Oxford, UK: Oxford University Press.
101. Emfietzoglou D, Moscovitch M. 2002 Inelastic collision characteristics of electrons in liquid water. *Nucl. Instrum. Methods Phys. Res. B* **193**, 71–78. (doi:10.1016/S0168-583X(02)00729-2)
102. Brini E, Fennell CJ, Fernandez-Serra M, Hribar-Lee B, Lukšiš M, Dill KA. 2017 How water's properties are encoded in its molecular structure and energies. *Chem. Rev.* **117**, 12 385–12 414. (doi:10.1021/acs.chemrev.7b00259)
103. Winter B, Weber R, Widdra W, Dittmar M, Faubel M, Hertel IV. 2004 Full valence band photoemission from liquid water using EUV synchrotron radiation. *J. Phys. Chem. A* **108**, 2625–2632. (doi:10.1021/jp030263q)
104. Prendergast D, Grossman JC, Galli G. 2005 The electronic structure of liquid water within density-functional theory. *J. Chem. Phys.* **123**, 014501. (doi:10.1063/1.1940612)
105. Dion M, Rydberg H, Schröder E, Langreth DC, Lundqvist BI. 2004 Van der Waals density functional for general geometries. *Phys. Rev. Lett.* **92**, 246401. (doi:10.1103/PhysRevLett.92.246401)
106. Román-Pérez G, Soler JM. 2009 Efficient implementation of a van der Waals density functional: application to double-wall carbon nanotubes. *Phys. Rev. Lett.* **103**, 096102. (doi:10.1103/PhysRevLett.103.096102)
107. Kühne TD *et al.* 2020 CP2K: an electronic structure and molecular dynamics software package—Quickstep: efficient and accurate electronic structure calculations. *J. Chem. Phys.* **152**, 194103. (doi:10.1063/5.0007045)
108. Koval NE, Koval P, Da Pieve F, Kohanoff J, Artacho E, Emfietzoglou D. 2022 Data from: Inelastic scattering of electrons in water from first principles: cross sections and inelastic mean free path for use in Monte Carlo track-structure simulations of biological damage. Dryad Digital Repository. (doi:10.5061/dryad.d51c5b057)